

SHOEMAKER-LEVY 9 IMPACT MODELING. I. HIGH-RESOLUTION THREE-DIMENSIONAL BOLIDES

D. G. KORYCANSKY

CODEP, Department of Earth Sciences, University of California, Santa Cruz, CA 95064; kory@pmc.ucsc.edu

JOSEPH HARRINGTON

Center for Radiophysics and Space Research, 326 Space Sciences Building, Cornell University, Ithaca, NY 14853-6801; jh@oobleck.astro.cornell.edu

DRAKE DEMING

NASA Goddard Space Flight Center, Planetary Systems Branch, Code 693, Greenbelt, MD 20771; ddeming@pop600.gsfc.nasa.gov

AND

MATTHEW E. KULICK

Center for Radiophysics and Space Research, 326 Space Sciences Building, Cornell University, Ithaca, NY 14853-6801; mek28@cornell.edu

Received 2005 November 7; accepted 2006 March 27

ABSTRACT

We have run high-resolution, three-dimensional, hydrodynamic simulations of the impact of comet Shoemaker-Levy 9 into the atmosphere of Jupiter. We find that the energy deposition profile is largely similar to the previous two-dimensional calculations of Mac Low & Zahnle, although perhaps somewhat broader in the range of height over which the energy is deposited. As with similar calculations for impacts into the Venusian atmosphere, there is considerable sensitivity in the results to small changes in the initial conditions, indicating dynamical chaos. We calculated the median depth of energy deposition (the height z at which 50% of the bolide's energy has been released) per run. The mean value among runs is ≈ 70 km below the 1 bar level, for a 1 km diameter impactor of porous ice of density $\rho = 0.6 \text{ g cm}^{-3}$. The standard deviation among these runs is 14 km. We find little evidence of a trend in these results with the resolution of the calculations (up to 57 cells across the impactor radius, or 8.8 m resolution), suggesting that resolutions as low as 16 grid cells across the radius of the bolide may yield good results for this particular quantity. Visualization of the bolide breakup shows that the ice impactors were shredded and/or compressed in a complicated manner but evidently did not fragment into separate, coherent masses, unlike calculations for basalt impactors. The processes that destroy the impactor take place at significantly shallower levels in the atmosphere (~ -40 km for a 1 km diameter bolide), but the shredded remains have enough inertia to carry them down another scale height or more before they lose their kinetic energy. Comparison of basalt impactor models shows that energy deposition curves for these objects have much less sensitivity to initial conditions than do ice impactors, which may reflect differences in the equation of state for the different kinds of objects, or a scale-dependent breakup phenomenology, with the preferred scale depending on impactor density. Models of impactors covering a ~ 600 -fold range of mass (m) show that larger impactors descend slightly deeper than expected from scaling the intercepted atmospheric column mass by the impactor mass. Instead, the intercepted column mass scales as $m^{1.2}$.

Subject headings: comets: individual (Shoemaker-Levy 9) — hydrodynamics

1. INTRODUCTION

For the week starting 1994 July 16, fragments of comet Shoemaker-Levy 9 (SL9) hit Jupiter. Most of the world's telescopes observed the event, collecting an unprecedented volume of imaging, photometry, and spectroscopy that spanned all sensible wavelengths. Papers in collections edited by West & Bönnhardt (1995) and Noll et al. (1996) review the data and early interpretation. Harrington et al. (2004) review the phenomenology, efforts to understand the impact phenomena, and open questions about the impacts. A brief summary of points relevant to this paper follows.

The impacts followed the same basic phenomenology. The orbital path of the comet fragments intersected the planetary surface at $\sim S45^\circ$ latitude, and planetary rotation arranged for a girdle of well-separated impacts there. Each impactor fell into the atmosphere at over 60 km s^{-1} and an impact angle of about 45° (Chodas & Yeomans 1996). The ground track of the impactors moved toward the northwest. The bolides crushed, ablated,

and decelerated as they fell through the atmosphere, leaving an entry channel filled with superheated gas (e.g., Ahrens et al. 1994a, 1994b; Boslough et al. 1995; Boslough & Gladstone 1997; Crawford 1996; Crawford et al. 1994; Mac Low 1996; Mac Low & Zahnle 1994; Takata et al. 1994; Takata & Ahrens 1997; Shuvalov et al. 1999). This gas rushed back out the entry channel, exiting the atmosphere at an angle and flying ballistically into space. The *Hubble Space Telescope* (*HST*) resolved the plumes and saw several rise to ~ 3000 km above the cloud tops (Hammel et al. 1995). Material invisible from Earth rose higher still, as shown by its effects on the magnetosphere (Brecht et al. 1995, 2001). The plumes collapsed and reentered the atmosphere in 20 minutes, heating it and leading to infrared emission so strong that it was dubbed the “main event.” In the initial hours after impact, two different systems of expanding rings were seen, one in the visible by *HST* (Hammel et al. 1995) and the other in the infrared by McGregor et al. (1996). Peculiar patterns remained in the atmosphere, which were spread in latitude over the ensuing weeks (Banfield et al. 1996).

Chemistry was just as exciting. Main-event spectra were complex, but only five species were identified. Dozens appeared in the aftermath, and CO and CO₂ are observed to this day, now having crossed the equator into the northern hemisphere (Bézard et al. 2002; Lellouch et al. 2002). Not to be outdone, the magnetosphere responded strongly and in a manner that changed throughout the week of impacts as ionized plume material loaded Jupiter’s magnetic field lines.

Initially viewed as perfect perturbation experiments, the impacts instead involved complex phenomena at fine spatial and temporal timescales. Models capable of reproducing many of the observed phenomena were too complex by several orders of magnitude for the computational power available at the time. Many observers, including most spectroscopists, still have unpublished data that they cannot interpret.

We made some headway in explaining phenomena of the images and light curves with simplified calculations. Harrington & Deming (2001) extrapolated a published blowout velocity distribution to calculate the fluxes of mass, energy, and momentum on the atmosphere. Deming & Harrington (2001) used those fluxes to drive a two-dimensional (2D) vertical slice model of the atmosphere. The resulting light curves are a good match to data from 0.9 to 12 μm , and the time-dependent pressure (p) and temperature (T) grids show phenomena that mimic McGregor’s ring and other effects.

Encouraged by this initial success, we have undertaken a study to model the impacts and their aftermath sufficiently to reproduce, in a realistic manner, all of the observed phenomena in the impact, blowout, plume flight, and plume splash phases. By “realistic,” we mean that wherever we can eliminate an ad hoc assumption or an analytic approximation, we do. We no longer use arbitrary initial conditions. Rather, we use observations and the results of prior models for initialization and ultimately produce synthetic images, light curves, and spectra derived with radiative transfer from model results. For physical atmospheric effects, our approach is to chain hydrodynamic models outlined by Harrington et al. (2004). Our chemical models are driven by tracer particle histories from the physical models.

This paper presents the first results from our impact model. Since the observations of this phase were not as constraining as those of later phases, our primary goal was to produce a data grid with which to initialize subsequent models. Doing this believably required a look at, e.g., resolution convergence and sensitivity to initial conditions. As with any interesting investigation, there are also serendipitous findings that reach beyond this particular set of impacts.

Korycansky et al. (2002) and Korycansky & Zahnle (2003) have made three-dimensional (3D) calculations of the impact of asteroids into the atmosphere of Venus using ZEUS-MP and its predecessor ZEUS3D. There are a number of similarities between the results of that work and the present study that we note below. Comparable hydrodynamical simulations of the initial phase of the impacts have been previously described by a number of groups (Boslough et al. 1994; Crawford et al. 1994, 1995; Gryaznov et al. 1994; Takata et al. 1994; Yabe et al. 1994, 1995; Shoemaker et al. 1995; Svetsov 1995; Crawford 1997; Shuvalov et al. 1997, 1999).

Section 2 presents our model. We describe the results of over a dozen runs in § 3 and discuss their implications and future work in § 4.

2. IMPACT MODEL

For the calculations described in this paper we employed the ZEUS-MP hydrodynamics code (Norman 2000), which solves

the equations for 3D compressible gas flow. We have modified ZEUS-MP (base ver. 1.0) to include multiple materials. Modifications to the code are described in more detail by Korycansky et al. (2002) and Korycansky & Zahnle (2003). We have not included radiative transfer in ZEUS-MP; the short timescale and high optical depth of the atmosphere below 1 bar, where the main disruption of the impactors and energy deposition takes place, make it unlikely that radiative transfer would significantly affect the dynamics. That assumption has been tested by Shuvalov et al. (1999), who indeed found that dynamical effects of radiation transfer were insignificant, but that the impacting comets would be strongly heated at large depths.

The Jovian atmospheric profile comes from Deming & Harrington (2001). We also included minor modifications, such as a moving grid that tracks the impactor at a variable velocity as it decelerates. Multiple materials were handled by the integration of tracer variables advected in the flow. For nonporous material, the tracer C gives the fraction of mass in the cell that is impactor material. Porosity is tracked by an additional tracer and is treated with the so-called p - α model for a strengthless, porous solid (Menikoff & Kober 1999). The coordinate system (x_1 , x_2 , and x_3) is Cartesian and aligned with the bolide’s initial velocity such that x_1 is the along-track coordinate, x_2 is horizontal, and x_3 is perpendicular to the others. We relate (x_1 , x_2 , and x_3) to local Cartesian coordinates (x , and y , z) as follows:

$$x = x_2, \quad (1)$$

$$y = -x_1 \sin \theta + x_3 \cos \theta, \quad (2)$$

$$z = x_1 \cos \theta + x_3 \sin \theta, \quad (3)$$

where θ is the angle between x_1 and the vertical. Note that local coordinates are not cardinal directions. Fluid velocities in the x_1 , x_2 , and x_3 directions are v_1 , v_2 , and v_3 , respectively. Other quantities that appear in the equations are the density, ρ and the internal energy per unit volume, e . The spatial resolution of the calculations is described by the notation Rn , where n is the number of grid cells across the radius of the body in the high-resolution part of the grid. Away from an inner block of dimensions $4 \times 2 \times 2$ km, the grid spacing increases geometrically (by a factor ~ 1.04 per grid cell, depending on the overall resolution). The computational grid moves with the impactor and decelerates, keeping the object’s front end about 1 km from the front end of the grid so that the object remains in the high-resolution portion as it disrupts. Calculations in the paper were made with resolutions of R16, R32, and R57.

We used the Tillotson equation of state (EOS), which was formulated for high-velocity impacts (Melosh 1989), although it cannot represent melting or mixed two-phase (gas-liquid) regimes. The Tillotson EOS has two regimes, one for cold and/or compressed material, the other for rarefied, hot conditions. For a given mass density of impactor material ρ and internal energy density (energy per unit volume) e , we have $\mathcal{E} = e/\rho$, $\eta = \rho/\rho_T$, and $q = \eta - 1$, where ρ_T is the density at zero pressure and \mathcal{E} is the specific energy. Then, for compressed states ($\eta > 1$) and expanded ones ($\eta < 1$), where $\mathcal{E} < \mathcal{E}_{iv}$, the incipient vaporization energy, the pressure P is the sum of a thermal term and a cold pressure term:

$$P = P_l = \left(a + \frac{b}{1 + \mathcal{E}/\mathcal{E}_T \eta^2} \right) e + \frac{Aq + Bq^2}{1 + e^{-K_c q}}. \quad (4)$$

The parameters a , b , A , B , and \mathcal{E}_T are described in more detail and listed for common substances by Melosh (1989); K_c is described

TABLE 1
TILLOTSON EOS PARAMETERS

Material	ρ_T (g cm ⁻³)	a	b	A (ergs cm ⁻³)	B (ergs cm ⁻³)	\mathcal{E}_T (ergs g ⁻¹)	\mathcal{E}_{iv} (ergs g ⁻¹)	\mathcal{E}_{cv} (ergs g ⁻¹)
Ice.....	0.917	0.3	0.1	9.47×10^{10}	9.47×10^{10}	1.0×10^{11}	7.73×10^9	3.04×10^{10}
Basalt.....	2.70	0.5	1.5	2.67×10^{11}	2.67×10^{11}	4.87×10^{12}	4.72×10^{10}	1.82×10^{11}

below. For expanded states for which $\mathcal{E} > \mathcal{E}_{cv}$, the energy of complete vaporization,

$$P = P_h = ae + \left(\frac{be}{1 + \mathcal{E}/\mathcal{E}_T\eta^2} + \frac{Aq}{1 + e^{-K_c q}} \right) e^{-5(1/\eta-1)^2}. \quad (5)$$

We modify the cold pressure terms $Aq + Bq^2$ and Aq in equations (4) and (5), respectively, by a term of the form $1 + e^{-K_c q}$ in the denominator, in order to provide a low-density cutoff as recommended by Melosh (1989). We set $K_c = 1000$. A strengthless material is assumed, so negative pressures (tensions) are not sustainable; the pressure cutoff for low densities mimics that effect. For expanded states in which $\mathcal{E}_{iv} < \mathcal{E} < \mathcal{E}_{cv}$, P is linearly interpolated between P_l and P_h . Then, on the grid, the resulting Tillotson pressure is weighted by the tracer C . The equation of state parameters for our materials (ice and basalt) are the same as used by Benz & Asphaug (1999) and are listed in Table 1. (As discussed below, we modeled basalt impactors in order to study the effect of the equation of state on impactor breakup.)

For porosity, we use a simple model for a strengthless, porous solid based on the p - α formulation (Herrmann 1969; Menikoff & Kober 1999). We distinguish between the solid material density ρ_m (and energy e_m) and the same quantities for fluid in the porous void space (ρ_p and e_p). Space and material quantities are related by the porosity ϵ , where $0 < \epsilon < 1$: $\rho = (1 - \epsilon)\rho_m$ and $e = (1 - \epsilon)e_m$. The material pressure p_m is provided by the equation of state $p_m(\rho_m, e_m)$ (the Tillotson EOS described above) and the space pressure is thus $p = (1 - \epsilon)p_m$. Initially the porosity is $1 - (\text{initial density/nominal density})$ of the material. During the calculation, porosity is advected with the flow like the material tracer C . At each time step the advected value of ϵ is then adjusted by comparison with a function $\epsilon_f(p, p_c) = \epsilon_0(1 - p/p_c)^2$ that depends on a “crushing pressure,” p_c , which for ice we set to 10^7 dyne cm⁻². For $p > p_c$, $\epsilon_f = 0$. The porosity is given by $\epsilon = \min(\epsilon, \epsilon_f)$. During the calculation, porosity can only decrease from its initial value; if porosity is crushed out of a mass element, it does not return even if the pressure drops back below p_c .

The Tillotson EOS has been used for SL9 calculations by Gryaznov et al. (1994) and Takata et al. (1994). Other equations of state for cometary material used in previous calculations include perfect gas (with adiabatic indices $\gamma = 1.2$ and 1.4 ; Mac Low 1996), and a “stiffened gas” or Murnaghan EOS with an additional perfect gas thermal contribution (Mac Low & Zahnle 1994). A similar stiff equation of state was used by Yabe et al. (1994, 1995). Boslough et al. (1994), Crawford et al. (1994, 1995), and Crawford (1997) used a tabular version of the ANEOS equation of state that took into account melting and vaporization. Shuvalov et al. (1999) used a combination of a nonlinear Gruneisen EOS in which the pressure increased roughly as the cube of the density ratio ρ/ρ_T combined with a tabular gas EOS for the vaporized component.

The most important factors in the various equations of state are probably the relative stiffness $dP/d\rho$ and whether the pressure depends on the internal energy e . A relatively stiff EOS, and one

in which P is also a function of e , might be expected to result in calculations that show impactors blowing up at greater altitudes and exhibiting more radial spreading (“pancaking”) than otherwise. This may explain some of the differences among the results that have been found from different studies. We do not systematically explore that question in this paper, but in view of the differences we found (discussed below) in results between ice and basalt impactors, we plan to address the issue in future work.

Our “standard case” is a 1 km diameter, porous ice sphere impacting the atmosphere at $v = 61.46$ km s⁻¹ and $\theta = 43^\circ.09$. The velocity and impact angle are the means of those of the 21 comet fragments (Chodas & Yeomans 1996) in a frame rotating with Jupiter at the average latitude of the impacts ($-44^\circ.02$). The gravitational acceleration at that latitude (including the J2 and centrifugal terms) is $g = 2512$ cm s⁻². The bulk density of the bolide is $\rho = 0.6$ g cm⁻³ (Asphaug & Benz 1994, 1996; Solem 1994, 1995).

We have also carried out calculations of impacts with objects of bulk density $\rho = 0.1$ and 0.92 g cm⁻³, the latter corresponding to nonporous solid ice. In addition, we have done calculations with impactors with volumes of 0.2, 3, 40, and 125 times that of the standard case, or diameters of 0.584, 1.44, 3.42, and 5 km. Not all combinations of density, diameters, and resolutions were run.

One important result that emerged from the Venusian atmosphere calculations was the significant extent to which the results were sensitively dependent on initial conditions in a manner reminiscent of dynamical chaos (Korycansky & Zahnle 2003). Two calculations whose initial conditions (for instance, impact velocity) differed by very small amounts ($\sim 0.1\%$) would develop large divergences in the course of their respective simulations. Korycansky et al. (2000) took the view that the basic process of impactor disruption was due to the growth of Rayleigh-Taylor and Kelvin-Helmholtz instabilities (Field & Ferrara 1995), and it is plausible that the seeds of the perturbations that grow to saturation are irregularities due to the finite resolution on the grid. In the physical case, one would expect analogous irregularities from the inevitable bumpiness of the bolide’s surface. While the basic process (fragmentation and ablation) was always the same, there could be significant differences in the results of different runs for impactors of the same gross properties. For example, the diameter of the resulting crater on the surface of Venus might vary by several kilometers (on a scale of ~ 10 km), depending on the exact details of how the event had unfolded. In the limit where the bolide just reached the surface, different cases might result in anything from a single crater several km in diameter, a group of small craters, or no crater at all. We might expect similar behavior to obtain in this case, and we have attempted to sample the distribution of results by performing several runs of the standard case with small differences in initial impact velocity Δv of 0.1% of the initial velocity v (≈ 0.06 km s⁻¹) or displacements in the cross-track coordinates $\Delta x_2, \Delta x_3$ by one-half a grid cell. For R16 calculations of the 1 km bolide the displacements are 15 m, for R32 they are 7.5 m, and for R57 they are 4.4 m.

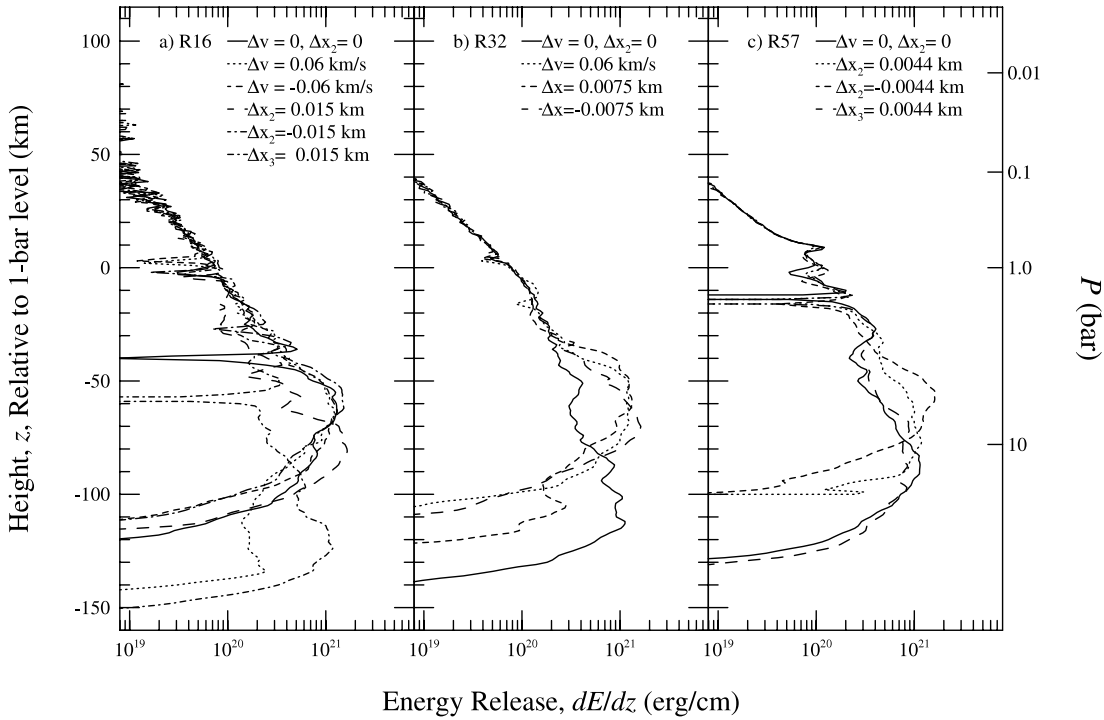


FIG. 1.— Energy deposition profiles for realizations of the impact of a 1 km diameter ice sphere ($\rho = 0.6 \text{ g cm}^{-3}$) into Jupiter's atmosphere at 61.4 km s^{-1} . Calculations at three different resolutions (R*n*; see text) are shown. (a) R16, Initial velocities differing by $\Delta v = 0.06 \text{ km s}^{-1}$ or initial positions displaced by 0.015 km from the standard case; (b) R32, initial velocities differing by $\Delta v = 0.06 \text{ km s}^{-1}$ or initial positions displaced by 0.0075 km from the standard case; (c) R57, initial positions displaced by 0.0044 km from the standard case.

We use several diagnostics to characterize the calculations. The simplest and most significant is the profile of deposition of impactor kinetic energy dE/dz as a function of height z in the atmosphere, the same quantity discussed by Mac Low & Zahnle (1994) and Mac Low (1996). The impactor kinetic energy $E = E(z)$ was calculated by integrating the flux of kinetic energy passing through a given height z :

$$E(z) = \int dt \int \int_z \rho C \frac{v_1^2 + v_2^2 + v_3^2}{2} v_1 dx_2 dx_3. \quad (6)$$

The area integral is taken over all cells whose height $z = x_1 \cos \theta + x_3 \sin \theta$ is the desired value. [Note that the projection factors $\cos \theta$ in the element of area in the z -plane ($dA = dx_2 dx_3 / \cos \theta$) and the downward velocity ($v_z = v_1 \cos \theta$) cancel.] The time integral extends to the end of the calculation (typically 8–10 s). The density on the grid is weighted by the advected tracer field C that tags material that belongs to the impactor. We computed $E(z)$ for $-200 \text{ km} \leq z \leq 100 \text{ km}$ at 1 km intervals. [For more massive bolides, $E(z)$ was calculated as far down as needed.] Having integrated $E(z)$ for all heights, the deposition profile dE/dz follows by numerical differentiation.

For a subset of the runs, we calculated spatially resolved plots of mass flux, similar to those employed by Korycansky & Zahnle (2004) to study the fragmentation of asteroids in the Venusian atmosphere. Here we hope to correlate events such as fragmentation, as revealed in the mass-flux plot, to specific features (like peaks) in the deposition profile.

The time-integrated mass flux $\mu(z; x, y)$ at a height z is given by

$$\mu(z; x, y) = - \int \rho(z; x, y) C(z; x, y) v_1(z; x, y) dt, \quad (7)$$

where z translates to the tilted plane $x_1 \cos \theta + x_3 \sin \theta$ in the grid coordinate system. In practice, μ is calculated as the accumulation of a set of integrals at time slices t_i , each integrated over the interval $t_i - \Delta t_i / 2$ to $t_i + \Delta t_i / 2$, by assuming that material moves at a constant velocity during that interval and counting all the mass that has crossed or will cross the plane during the interval. Due to the tilt of the grid, the y -location of the impactor is a function of z ; in this case we refer the position of material on the plane to the center line position defined by $x_2 = x_3 = 0$.

The calculations were performed on a Beowulf cluster using 32 2.4 GHz Opteron processors. The largest (R57) runs took $\sim 3.1 \times 10^7$ CPU s on a grid of $712 \times 356 \times 356 = 9.0 \times 10^7$ points. Impactors of 1 km diameter took ~ 8 – 10 model seconds for the velocity to fall to 0.001 times the initial velocity, which was the condition for stopping the calculation. Time steps were $\sim 5 \times 10^{-5}$ s during the initial phases of the impact, increasing to $\sim 3 \times 10^{-4}$ s by the end, as the impactor slowed down. High-resolution output was written to disk every 0.1 model seconds, as noted above. The R57 calculations occupied 17 GB of memory and produced ~ 210 GB of output data. Not all data were saved from all runs. Wall clock time for an R57 run was about 3 weeks.

3. RESULTS

Our main results are presented in Figures 1 and 2, which show the profile of kinetic energy deposition (dE/dz) for a number of realizations of the standard case described above. Figures 1 and 2 show much the same information, plotted in two different ways to emphasize two different points. Each panel shows profiles generated by calculations with very slight differences in initial conditions, as described above. The panels show calculations done at different resolutions: R16, R32, and R57. In Figure 1, the horizontal scale is logarithmic, to facilitate a

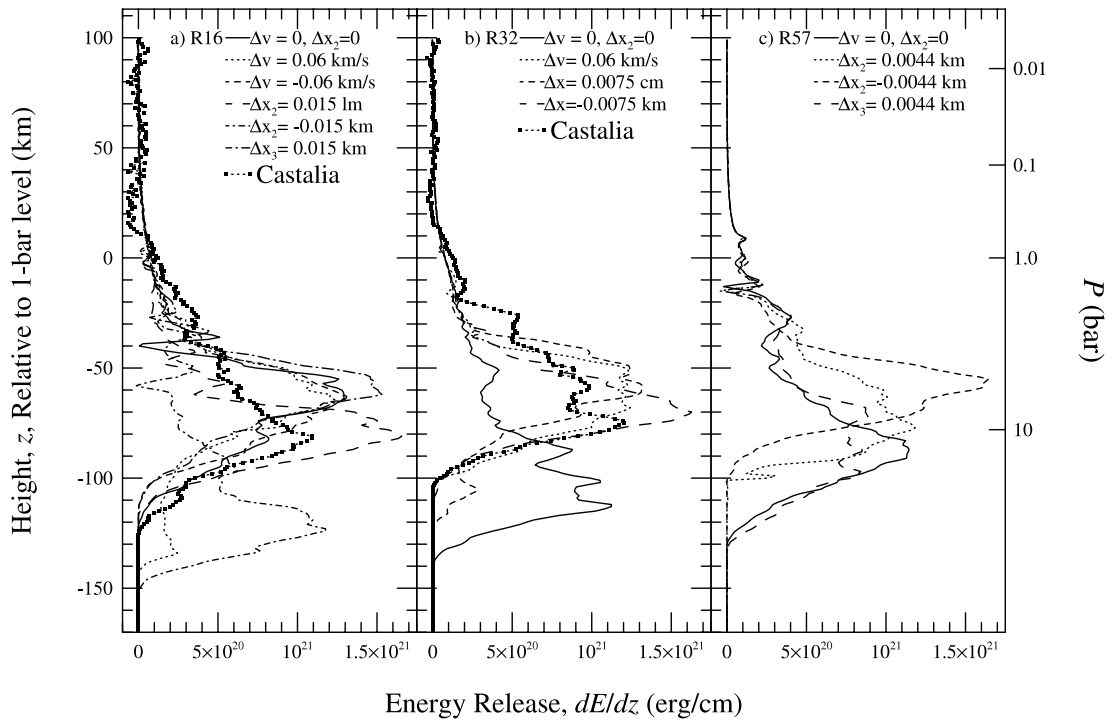


FIG. 2.— Same as Fig. 1, but now with a linear scale on the horizontal axis that emphasizes the differences in energy deposition among the runs. Also included among the plotted runs are two calculations (at resolutions R16 and R32) of impactors shaped like the asteroid 4769 Castalia. Both these runs fall among the main group of runs at each resolution, indicating that initial macroscopic impactor shape does not strongly affect energy deposition behavior.

comparison to the results of Mac Low & Zahnle (1994) and Crawford (1996).

For the most part previous calculations have been 2D axisymmetric calculations at moderately high resolutions (R25) with finite-difference (grid based) hydrocodes. The exception is the calculation by Takata et al. (1994), a 3D calculation employing the smooth particle hydrodynamics (SPH) method. Several groups found that a 1 km object penetrated more deeply than we found, to depths well below -100 km, $P > 15$ bar (Boslough et al. 1994; Crawford et al. 1994, 1995; Takata et al. 1994). Shuvalov et al. (1999) found different results, partly due to the different density and structure of the objects they model. Some of their calculations were made for an object of $\rho = 0.22$ g cm $^{-3}$. They also investigated the impacts of objects of nonuniform density: a dense core ($\rho = 1$ g cm $^{-3}$) and surrounding shell of low density ($\rho = 0.1$ g cm $^{-3}$) and a low-density object with high-density inclusions. Their objects had the same diameter (1 km), but were about 1/3 as massive as our standard object. Shuvalov et al. found a rather broad, double-peaked distribution of energy deposition. Our results are most similar to those of Mac Low & Zahnle (1994) and Crawford (1997). The energy release profile is sharply peaked, although not so strongly as found by Mac Low & Zahnle; a small amount of energy is deposited at levels below 100 km. It is apparent that the sensitivity to initial conditions described above also obtains for these simulations. This is brought out more strongly in Figure 2, in which the horizontal scale is linear.

An important question about simulations of this type is the degree of convergence that they exhibit as a function of numerical parameters such as resolution. In this case convergence means that extrapolation to infinite resolution of a series of models would yield a series of results that converged to the correct answer. Ideally, the limit of resolution-independent results is reached while we are still in the realizable limit of finite

resolution. The question in this case is complicated by the sensitivity to initial conditions discussed above, since a degree of scatter in the results is introduced, as can be seen in Figure 2. The scatter tends to obscure trends in the results as a function of resolution. We must thus compare the results as a function of resolution on a statistical basis.

Also included among the runs plotted in Figure 2 are two calculations (at resolutions R16 and R32) of bolides shaped like the asteroid 4769 Castalia, but with the same volume and density as our standard case. These runs are a test of the influence of the bolide's shape on the outcome, the object being in these cases an oblong object with axis ratios 2:1:0.8 and perhaps a representative shape for nonspherical impactors. The object in these cases was oriented end-on to the direction of motion. The particular model shape was already available for use, having been extensively used in the calculations performed by Korycansky & Zahnle (2003). The results of the runs of Castalia-shaped impactors do not appear to be radically different from spherical ones. Large changes in impactor shape do not seem to affect the outcome more than tiny changes in the initial position or velocity. Presumably, very extreme shapes (e.g., needle-like or plate-shaped objects) would have an effect, but moderately oblong shapes are not a strong influence. For a relatively fragile impactor, it is probably true that the initial shape is quickly "forgotten" as the incoming object is rapidly deformed by aerodynamic forces and that the same effects that apply to our spherical impactors also apply here. We expect that a sequence of calculations for irregular objects with small changes in initial conditions would show a similar degree of scatter in the results. Crawford et al. (1995) also simulated the impact of 2D, nonspherical objects (cylinders with length/diameter ratios of 1:3 and 3:1) and found a significant but not overwhelming dependence on body shape; paradoxically, the 3:1, rod-shaped impactor penetrated the least deeply among the three cases tested.

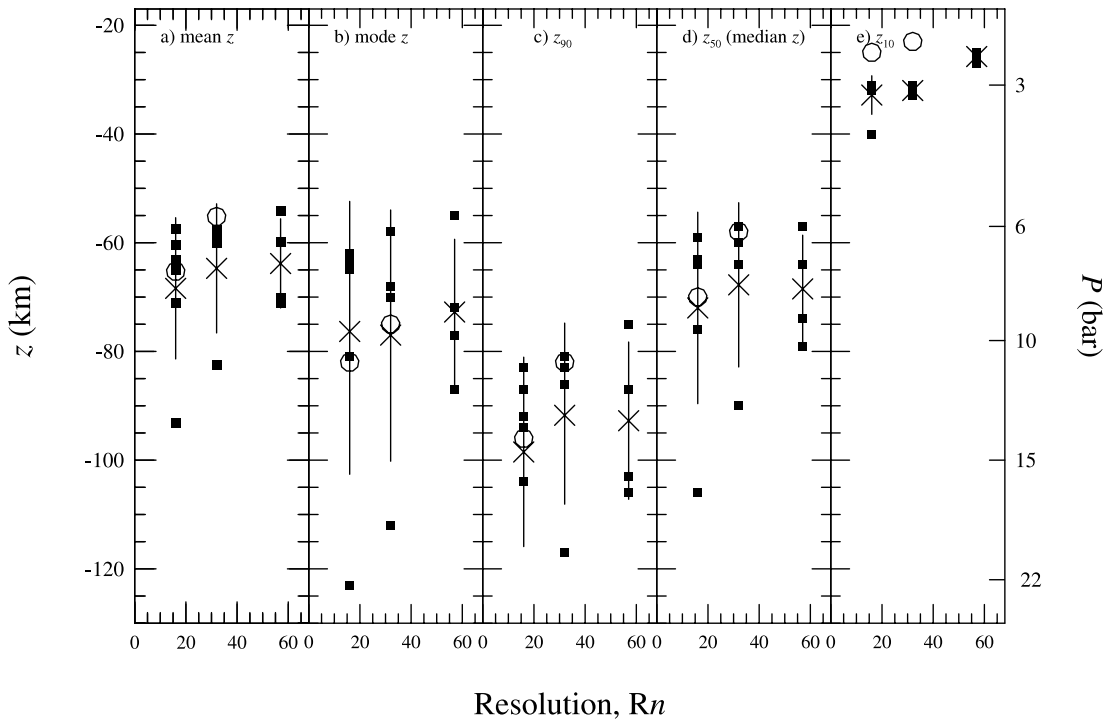


FIG. 3.—Measures of energy deposition for the runs shown in Fig. 1. Squares refer to individual runs whose curves are plotted in Fig. 1 at resolutions R16, R32, and R57. The horizontal coordinate in each panel is the resolution. Crosses are the means of the runs at a given resolution, and the vertical line extends to ± 1 standard deviation of the distribution. The circles refer to the results of the Castalia-shaped bolides. (a) Mean z -value of energy deposition, calculated from the first moments of the energy deposition profile; (b) mode z , or the depth of maximum energy deposition; (c–e) depth, at which 90%, 50%, and 10% the impact kinetic energy has been deposited.

Figure 3 shows various statistical measures of the energy deposition, in particular several different depths that characterize the results. Included in the plot are the mean depth [$\bar{z} = \int z(dE/dz) dz/E$] or the first moment of the energy deposition curve, the mode depth z (the depth of peak energy deposition), and the depths z_n at which $n\%$ of the bolide's energy has been deposited for $n = 90, 50,$ and 10 (z_{50} is the median depth). The mean and median depths are quite similar, despite the skewness of the deposition profiles, while the peak energy deposition depths z are somewhat deeper. The trend (if any) of these measures as a function of resolution is weaker than the amount of scatter, as seen by the standard deviation. In particular, the R57 runs give approximately the same results as the ones at lower resolution. Statistical tests (t - and F -tests) applied to the various measures of depth for R16 and R57 find that the differences between them are not statistically significant. However, the variance of the R16 results is 3–4 times larger than those of R57, and if the same results persisted after ~ 10 more cases were run, a significant result might emerge. That is, it is possible that the amount of scatter in the results is smaller for high-resolution runs. We also note that the results for the Castalia runs do appear to result in systematically slightly shallower depths than the means at R16 and R32. However, only one Castalia run was done for R16 and R32, so the apparent results may not be significant.

We also examined the spatially resolved, integrated fluxes $\mu(z; x, y)$ described in § 2. These provide clues as to exactly how an impact proceeds, in terms of understanding the processes of fragmentation, ablation, and impactor spreading due to aerodynamic forces (pressure gradients). The last process has been denoted “pancaking” (Zahnle 1992; Chyba et al. 1993) and has been modeled semianalytically and applied to SL9 impacts by several groups (Chevalier & Sarazin 1994; Zahnle & Mac Low 1994; Mac Low & Zahnle 1994; Field & Ferrara 1995; Crawford

1997). We do not make such a model in this paper, but simply discuss the hydrodynamical results.

Figure 4 shows the time-integrated flux $\mu(z; x, y)$ calculated at various heights z relative to the 1 bar level for the R57 run. The flux is plotted on a logarithmic gray scale for $\mu > 5 \times 10^2 \text{ g cm}^{-2}$, which emphasizes relatively small values of μ . Values of $5 \times 10^4 \text{ g cm}^{-2}$ and above are shown in the deepest shade (black). (For comparison, note that a column 1 km high of $\rho = 0.6 \text{ g cm}^{-3}$ has a surface density of $6 \times 10^4 \text{ g cm}^{-2}$.) Only the inner $4 \times 4 \text{ km}^2$ region of the projected grid is shown. Due to the zenith angle of the impact ($\approx 44^\circ$) the footprint of the impact is elongated in the $+y$ -direction in the plots; the effect is most noticeable in the $z = 20 \text{ km}$ plot, in which the bolide is not yet strongly affected by the atmosphere.

The object is torn apart quite high in the atmosphere (approximately between $z = -20$ and -50 km) compared to the region below -50 km , where most of the energy is deposited. Despite the explosion-like character of the impact, the crushed bolide has enough inertia to carry it down another scale height before it stops and deposits its kinetic energy. The same behavior was noted by Shuvalov et al. (1999) in their calculations.

In Figure 5 we show a quantity similar to μ for the R57 run, namely, the column density σ in the (x_1, x_3) plane, or a side view of the impactor generated by integrating the density of impactor material in the x_2 direction,

$$\sigma(x_1, x_3) = \int \rho C dx_2. \quad (8)$$

Note that σ is not time integrated; we show particular instants in the calculation when the bolide is passing through z -levels that are approximately the same as those shown in Figure 4. Note also that Figure 5 is plotted in grid coordinates $(x_1, \text{ and } x_3)$, which are

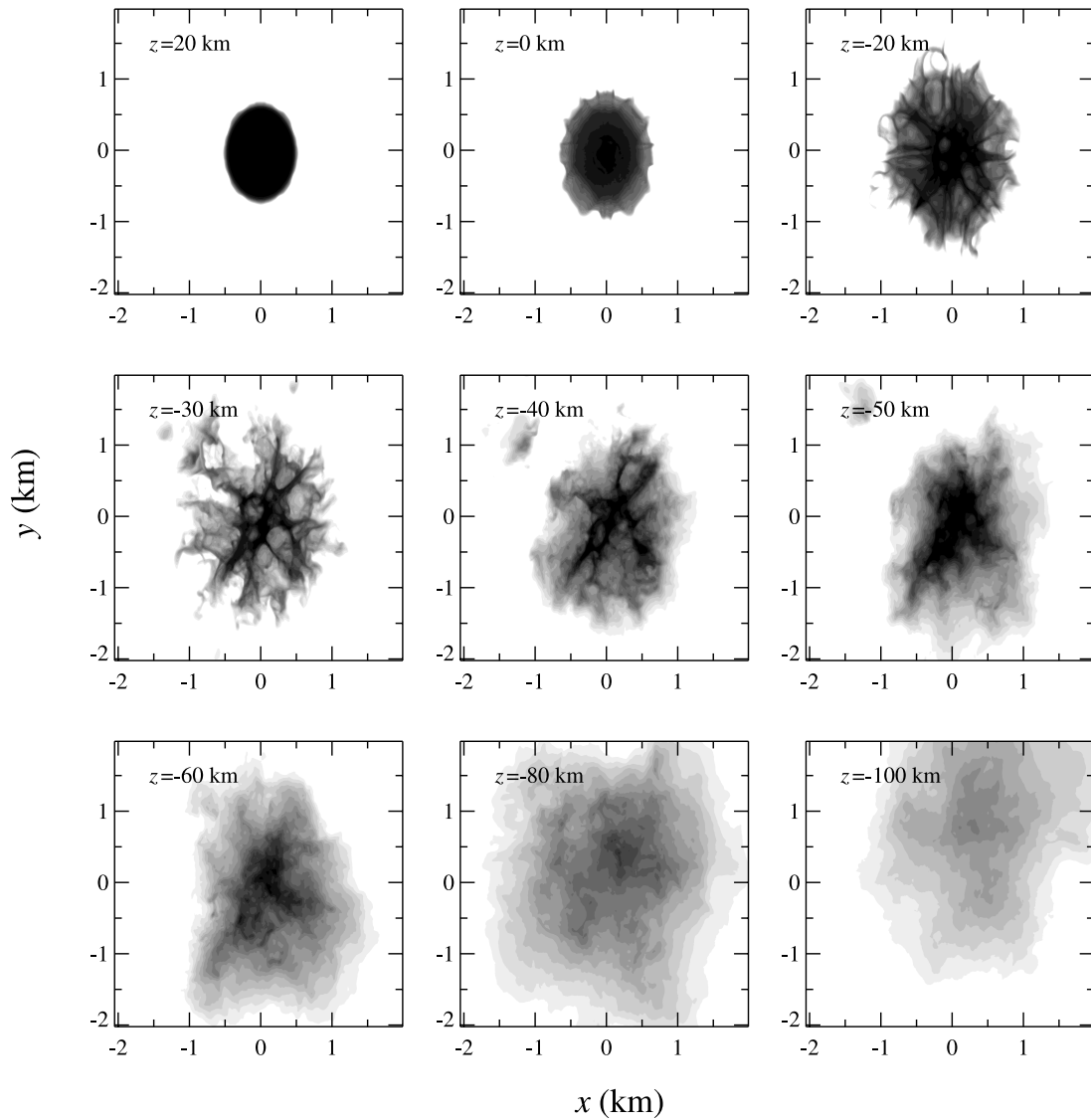


FIG. 4.— Time-integrated mass fluxes $\mu(z; x, y)$ as defined in eq. (7) for the R57 run at various heights z relative to the 1 bar level. The fluxes are plotted on a logarithmic gray scale for values of $\mu > 5 \times 10^2 \text{ g cm}^{-2}$, and the darkest shade (*black*) corresponds to $\mu > 5 \times 10^4 \text{ g cm}^{-2}$. Only a grid subsection is shown.

related to z by equation (3). Figure 5 shows the compression and disruption of the bolide from a different point of view. The most interesting part of Figure 5 is the initial compression of the bolide seen at $t = 2.7 \text{ s}$, followed by the shredding and sweeping back of material for $t > 3 \text{ s}$. As noted above for Figure 4, the lateral spreading of the impactor during its initial compression is not larger than a factor of 2 or so.

A notable feature is the character of the impactor disruption. The impactor is apparently shredded and crushed, but does not seem to fragment into large pieces that separate at significant velocity. Nonaxisymmetric filamentary structures develop and then expand into a cloud of material. This behavior is different from what has been seen in calculations of asteroid impacts into the atmosphere of Venus (Korycansky et al. 2002; Korycansky & Zahnle 2003) and inferred from craters on Venus (Korycansky & Zahnle 2004) and the Earth (Passey & Melosh 1980). Other calculations at lower resolution (R32 and R16) show similar behavior. Given that the same code was used for Venus calculations (Korycansky & Zahnle 2003) and the calculations are in many ways very similar, we conclude that the material of the bolide

(porous ice vs. rock) and its compressibility must control the character of impactor breakup in these physical situations.

To test this idea, we ran an R32 simulation of a 1 km spherical impactor of nonporous basalt ($\rho = 2.7 \text{ g cm}^{-3}$) with conditions otherwise identical to our standard case. The results are shown in Figure 6, where we compare an R32 porous ice calculation (*top row*) with the basalt impactor (*bottom row*) at selected heights in the atmosphere. Because the basalt bolide is ~ 5 times as massive as the ice one, it penetrates more deeply, as reflected in the choice of heights in Figure 6. Of more interest is the impactor breakup: the basalt object appears to break into several fragments and spread out (pancake) considerably more than does the ice impactor, whose degree of pancaking is rather modest, less than a factor of 2 in radius. However, to assess the degree to which the pancake model does or does not match the behavior seen in Figures 4–6 requires quantitative modeling that we postpone to future work.

Figure 7 shows an additional exploration of the possible outcomes due to differing substances. We ran five R16 impact calculations for 1 km diameter impactors of nonporous ice and porous

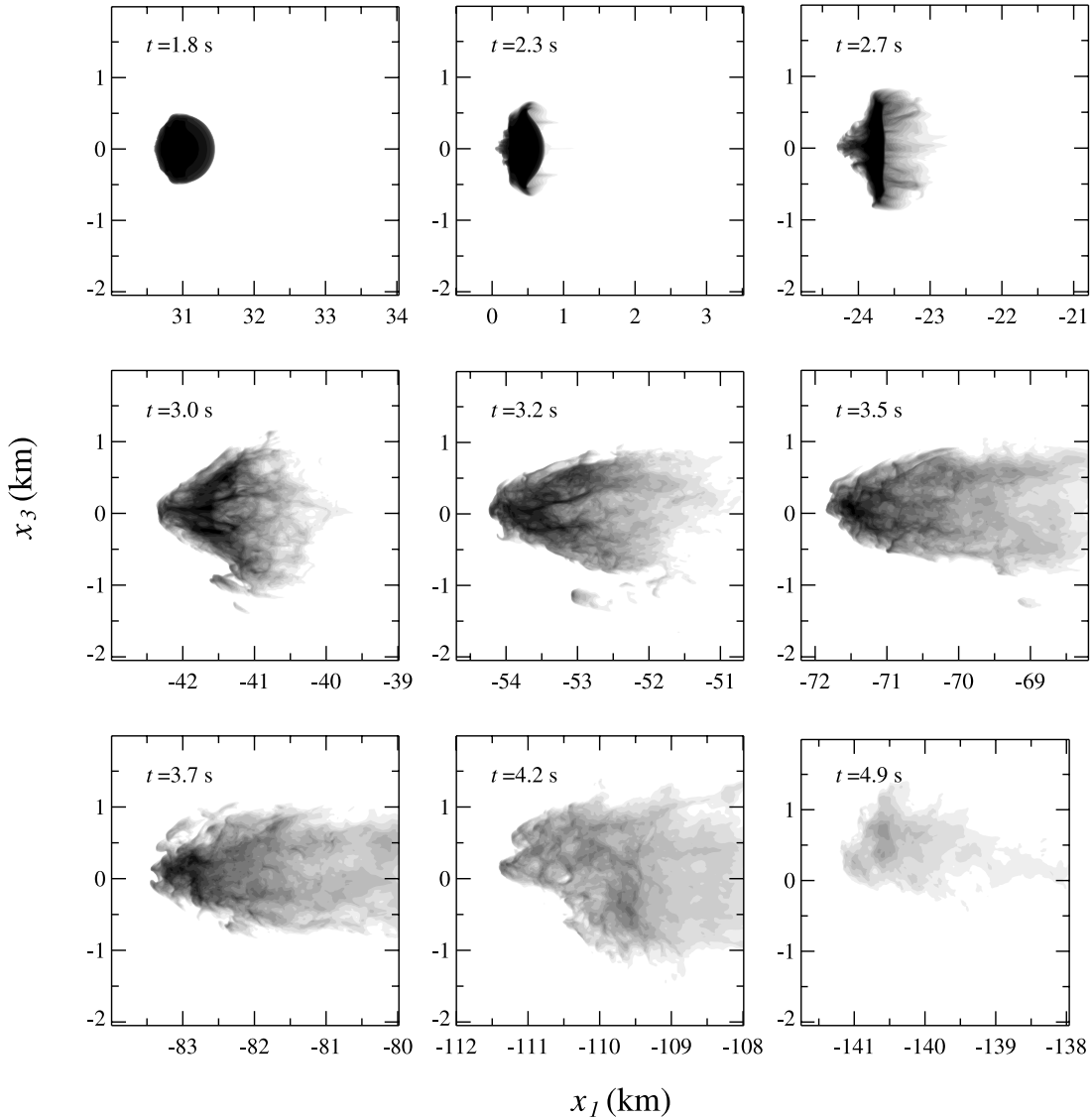


FIG. 5.— Column densities σ in the x_1 - x_3 plane (horizontal and vertical, respectively), for one R57 run. The times and heights roughly correspond to the passage of the bolide through the z -planes given in the same panels in Fig. 4. Shading is the same as for Fig. 4, substituting σ for μ . Only a grid subsection is shown.

and nonporous basalt. The differing impactor masses largely account for the variation of average penetration depth per impactor type. However, the differences in the shapes and the level of variation among different trials is unexpected. The difference in outcomes between ice and basalt is marked; the icy impactors show much greater variation in energy deposition (and a much greater overall spread in height) than do the basalt impactors. Differences in initial porosity seem to have little effect compared with the difference in material. Presumably this is due to differences in coefficients in the EOS. We speculate that the greater stiffness of the basalt EOS results in greater pancaking (as in Fig. 6) and (somewhat paradoxically) less variation in the disruption and energy deposition as a result. One way to examine the question is to run models with simplified and artificially stiffened or softened equations of state. Understanding this result would reveal fundamental impact physics and may enable simplified models of atmospheric impacts that do not require extensive hydrodynamic simulation. We hope to address this question in more detail in the future.

As noted above, we have also run simulations of the impact of bolides of differing masses corresponding to masses 0.2, 3, 40, and 125 times that of the standard case. The corresponding

diameters are 0.584, 1.44, 3.42, and 5 km. We ran five cases of each diameter at R16 resolution, perturbing the initial positions in x_2 and x_3 by one-half a grid cell. The results are shown in Figure 8, where we plot the median depths of energy deposition z_{10} , z_{50} , and z_{90} in the top panel as a function of bolide mass. The bottom panel shows the same result, but now we plot the corresponding atmosphere columns $\mu_{10,50,90} = \int_{z_{10,50,90}}^{\infty} \rho dz$ times the initial bolide cross section $A = \pi r^2$, normalized by the bolide mass m . Least-squares fits for z and μ are

$$z_{10} = -9.50 \times 10^{-4} (m/g)^{0.309} \text{ km}, \quad (9)$$

$$z_{50} = -5.19 \times 10^{-3} (m/g)^{0.283} \text{ km}, \quad (10)$$

$$z_{90} = -1.82 \times 10^{-2} (m/g)^{0.257} \text{ km}, \quad (11)$$

$$\frac{\mu_{10} A}{m} = 8.16 \times 10^{-3} (m/g)^{0.041}, \quad (12)$$

$$\frac{\mu_{50} A}{m} = 1.20 \times 10^{-4} (m/g)^{0.199}, \quad (13)$$

$$\frac{\mu_{90} A}{m} = 1.03 \times 10^{-4} (m/g)^{0.220}. \quad (14)$$

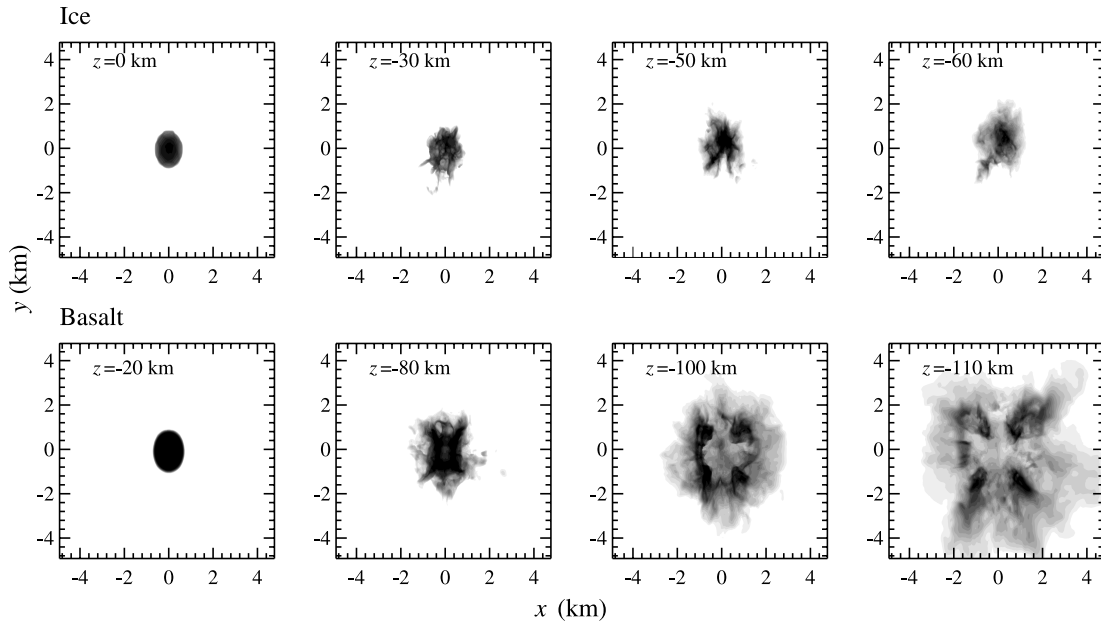


FIG. 6.— Time-integrated mass fluxes $\mu(z; x, y)$ as defined in eq. (7) for two R32 runs at various heights, z , relative to the 1 bar level. *Top row*, Ice impactor; *bottom row*, impactor of nonporous basalt ($\rho = 2.7 \text{ g cm}^{-3}$). Shading is the same as for Fig. 4. Only a grid subsection is shown, but it is larger than that in Fig. 4.

Note that the same sensitivity to initial conditions appears across a 600-fold range in impactor mass. We expect that impactors would in general penetrate to column depths equivalent to their mass, i.e., $\mu A \sim m$, as was found roughly to be the case by Korycansky & Zahnle (2003) for impacts into the Venusian atmosphere. Thus, we would expect $\mu A \propto m$. As seen in equation (14) there is a weak dependence on impactor mass. More massive impactors penetrate somewhat more deeply than would be expected from a strictly proportional relation.

4. CONCLUSIONS

To gain understanding of the SL9 impacts, we have carried out a number of 3D, hydrodynamic simulations of the impact of porous ice comets into the atmosphere of Jupiter. We employed the numerical hydrodynamics code ZEUS-MP, with some modifications to track the comet material (ice), its equation of state, and the degree of porosity, if present. Calculations were carried out at three different resolutions R_n , where n is the number of

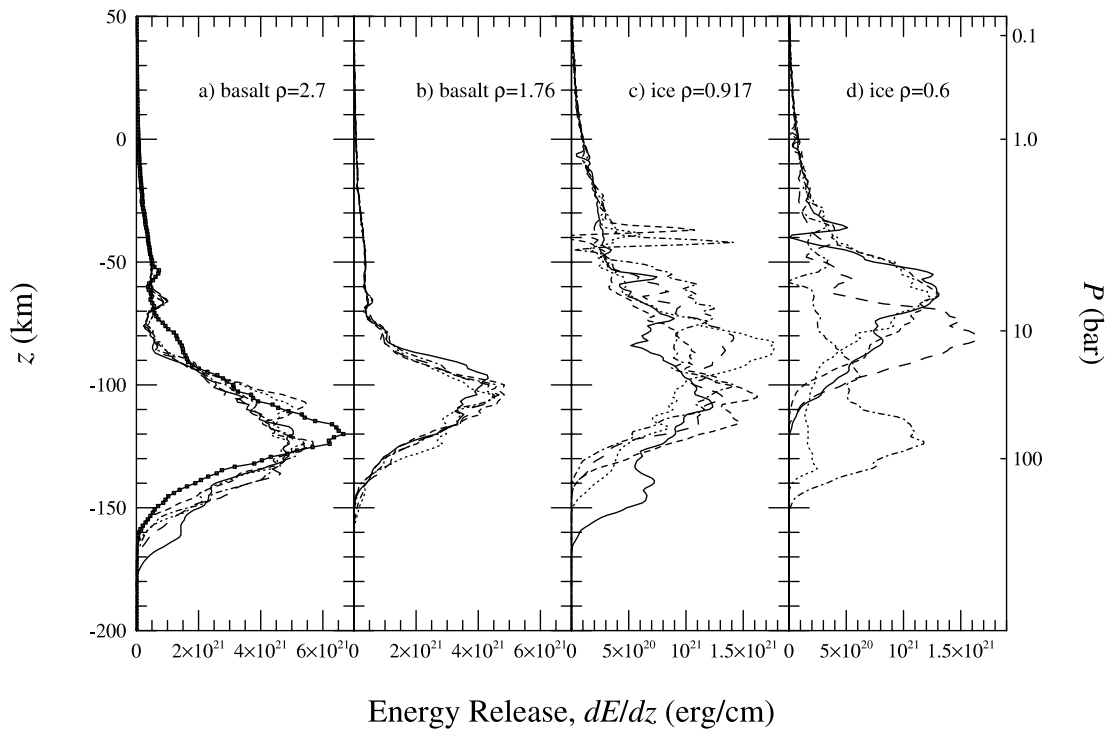


FIG. 7.— Energy deposition curves for basalt vs. ice and porous vs. nonporous 1 km diameter objects. Five R16 calculations with differences of 0.015 km in initial x_2 and x_3 positions are shown in each panel. (*a–b*) Basalt; (*c–d*) ice; (*b–d*) impactors of 35% initial porosity. Note the difference in horizontal scale for dE/dz between (*a*) and (*b*), and (*c*) and (*d*). (*d*) Same runs as in Figs. 1 and 2.

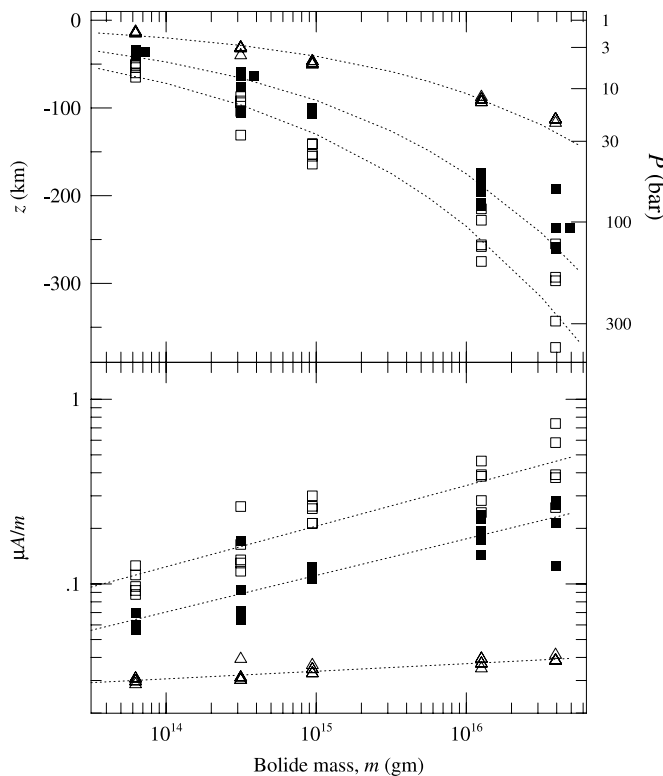


FIG. 8.—Depth of bolide penetration into the Jovian atmosphere as a function of bolide mass. *Top*: Depths of energy deposition z_{10} , z_{50} , and z_{90} for five R16 calculations with tiny perturbations to their initial positions. The dashed lines are fits to the results from eq. (14). Triangles show z_{10} , filled squares show z_{50} , and open squares show z_{90} . Impactor diameters are 0.584, 1.0, 1.44, 3.42, and 5 km. The dashed lines show fits to the results. *Bottom*: Atmosphere column times initial bolide cross section, μA , normalized to bolide mass, as a function of bolide mass, for 10%, 50%, and 90% levels of energy deposition. The dashed lines are fits to the results from eq. (14). Triangles show $\mu_{10}A/m$, filled squares show $\mu_{50}A/m$, and open squares show $\mu_{90}A/m$.

resolution elements across the bolide radius (for spherical impactors): R16, R32, and R57. We have paid special attention to the profile of energy deposition in the atmosphere, as a measure of how deeply the bolide penetrated and for comparison with previous (mostly 2D) simulations. We carried out several calculations of a standard case (a 1 km diameter, porous, ice comet with $\rho = 0.6 \text{ g cm}^{-3}$ and initial velocity like that of the SL9 impactors) with tiny variations in initial velocity or shifts in crosswise position on the computational grid, in order to test for sensitivity of the results to initial conditions and to sample the distribution of results if the sensitivity were present. Such multiple calculations were carried out at all three of our resolutions to see if there was a convergence trend in the results. Two low- and medium-resolution calculations of an impactor in the shape of the asteroid 4769 Castalia were also done to see if there were noticeable differences for a nonspherical impactor.

Energy deposition profiles were fairly similar to those found for 2D calculations such as those done by Mac Low & Zahnle (1994), although they were slightly less sharply peaked. The median depth of energy deposition was $\approx 70 \pm 14$ km below the 1 bar level, at an atmospheric pressure of ≈ 10 bars. The aforementioned sensitivity of the results to small changes in initial conditions produced significant variations in the energy deposition profiles, and the error bar just given refers to the standard deviation of the individual profiles. Comparing the results of calculations at different resolutions shows very little trend in the results, compared to their scatter. This suggests that, for the purpose of determining the depth of penetration of impactors, relatively low resolution (R16) is sufficient.

We have visualized some of the calculations to learn about the impact process and how a bolide responds to aerodynamic forces. The pictures we see are consistent with the pancake model of Zahnle (1992) and Chyba et al. (1993). The impactor is flattened quite strongly at early times, but the extent of radial spreading was no more than a factor of 2 in radius. Shortly thereafter, the impactor develops nonaxisymmetric structures and shreds into filamentary structures before coming apart completely. Material is blown back and outward as ablation proceeds until the impactor material expands into a cloud that slows down and deposits its kinetic energy into the atmosphere. The disruption takes place at a considerably shallower depth (at ~ -40 km) than the peak deposition of energy; the broken-up impactor material has sufficient inertia to be carried downward a significant distance (~ 1 scale height or more) before being stopped.

A set of “low resolution” (R16) runs of impactors over a 600-fold range in mass (corresponding to diameters $0.584 \text{ km} < d < 5 \text{ km}$) produced median depths of energy deposition ranging from 35 to ~ 250 km below the 1 bar level. Scaling the results by the amount of atmospheric mass intercepted by the bolide showed a weak dependence on impactor mass, with more massive bolides penetrating slightly more deeply than predicted by a linear relation between intercepted atmospheric column and bolide mass.

Future work will extend these results in a number of directions. We will explore the parameter space of impactor mass and composition. High-resolution calculations will also serve as the basis for new models of the impactor plume and splashback that generated the greater part of the SL9 phenomena observed from Earth. The results of these calculations will also serve as input for simplified, semianalytic, general models of atmospheric impacts for diverse situations such as impacts on the atmospheres of Earth, Venus, and Titan.

We thank K. Zahnle for useful discussions, and the referee, M.-M. Mac Low, for helpful suggestions. This material is based on work supported by the National Science Foundation under grant 0307638 and on work supported by the National Aeronautics and Space Administration under grant NNG 04GQ35G issued through the Science Mission Directorate.

REFERENCES

- Ahrens, T. J., Takata, T., O’Keefe, J. D., & Orton, G. S. 1994a, *Geophys. Res. Lett.*, 21, 1087
 ———. 1994b, *Geophys. Res. Lett.*, 21, 1551
 Asphaug, E., & Benz, W. 1994, *Nature*, 370, 120
 ———. 1996, *Icarus*, 121, 225
 Banfield, D., Gierasch, P. J., Squyres, S. W., Nicholson, P. D., Conrath, B. J., & Matthews, K. 1996, *Icarus*, 121, 389
 Benz, W., & Asphaug, E. 1999, *Icarus*, 142, 5
 Bézard, B., Lellouch, E., Strobel, D., Maillard, J.-P., & Drossart, P. 2002, *Icarus*, 159, 95
 Boslough, M. B., Crawford, D. A., Robinson, A. C., & Trucano, T. G. 1994, *Geophys. Res. Lett.*, 21, 1555
 Boslough, M. B., Crawford, D. A., Trucano, T. G., & Robinson, A. C. 1995, *Geophys. Res. Lett.*, 22, 1821
 Boslough, M. B. E., & Gladstone, G. R. 1997, *Geophys. Res. Lett.*, 24, 3117
 Brecht, S. H., de Pater, I., Larson, D. J., & Pesses, M. E. 2001, *Icarus*, 151, 25

- Brecht, S. H., Pesses, M., Lyon, J. G., Gladd, N. T., & McDonald, S. W. 1995, *Geophys. Res. Lett.*, 22, 1805
- Chevalier, R. A., & Sarazin, C. L. 1994, *ApJ*, 429, 863
- Chodas, P. W., & Yeomans, D. K. 1996, in *IAU Colloq. 156, The Impact of Comet Shoemaker-Levy 9 on Jupiter*, ed. K. S. Noll, H. A. Weaver, & P. D. Feldman (Cambridge: Cambridge Univ. Press), 1
- Chyba, C. F., Thomas, P. J., & Zahnle, K. J. 1993, *Nature*, 361, 40
- Crawford, D. A. 1996, in *IAU Colloq. 156, The Impact of Comet Shoemaker-Levy 9 on Jupiter*, ed. K. S. Noll, H. A. Weaver, & P. D. Feldman (Cambridge: Cambridge Univ. Press), 133
- . 1997, *Ann. NY Acad. Sci.*, 822, 155
- Crawford, D. A., Boslough, M. B., Trucano, T. G., & Robinson, A. C. 1994, *Shock Waves*, Vol. 4, 47
- . 1995, *Int. J. Impact Eng.*, 17, 253
- Deming, D., & Harrington, J. 2001, *ApJ*, 561, 468
- Field, G. B., & Ferrara, A. 1995, *ApJ*, 438, 957
- Gryaznov, V. K., Ivanov, B. A., Ivlev, A. B., Klumov, B. A., Utyuzhnikov, S. V., & Fortov, V. E. 1994, *Earth Moon Planets*, 66, 99
- Hammel, H. B., et al. 1995, *Science*, 267, 1288
- Harrington, J., de Pater, I., Brecht, S. H., Deming, D., Meadows, V. S., Zahnle, K., & Nicholson, P. D. 2004, in *Jupiter: The Planet, Satellites, and Magnetosphere*, ed. F. Bagenal, T. E. Dowling, & W. B. McKinnon (Cambridge: Cambridge Univ. Press), 159
- Harrington, J., & Deming, D. 2001, *ApJ*, 561, 455
- Herrmann, W. 1969, *J. Appl. Phys.*, 40, 2490
- Korycansky, D. G., & Zahnle, K. J. 2003, *Icarus*, 161, 244
- . 2004, *Icarus*, 169, 287
- Korycansky, D. G., Zahnle, K. J., & Mac Low, M.-M. 2000, *Icarus*, 146, 387
- . 2002, *Icarus*, 157, 1
- Lellouch, E., et al. 2002, *Icarus*, 159, 112
- Mac Low, M.-M. 1996, in *IAU Colloq. 156, The Impact of Comet Shoemaker-Levy 9 on Jupiter*, ed. K. S. Noll, H. A. Weaver, & P. D. Feldman (Cambridge: Cambridge Univ. Press), 157
- Mac Low, M.-M., & Zahnle, K. 1994, *ApJ*, 434, L33
- McGregor, P. J., Nicholson, P. D., & Allen, M. G. 1996, *Icarus*, 121, 361
- Melosh, H. J. 1989, *Impact Cratering: A Geologic Process* (New York: Oxford Univ. Press), 45
- Menikoff, R., & Kober, E. 1999, in *APS Abstr. Topical Conference on Shock Compression in Condensed Matter* (New York: APS)
- Noll, K. S., Weaver, H. A., & Feldman, P. D., eds. 1996, *IAU Colloq. 156, The Impact of Comet Shoemaker-Levy 9 on Jupiter* (Cambridge: Cambridge Univ. Press)
- Norman, M. L. 2000, *Rev. Mex. AA Ser. Conf.*, 9, 66
- Passey, Q. R., & Melosh, H. J. 1980, *Icarus*, 42, 211
- Shoemaker, E. M., Hassig, P. J., & Roddy, D. J. 1995, *Geophys. Res. Lett.*, 22, 1825
- Shuvalov, V. V., Artem'eva, N. A., & Kosarev, I. B. 1999, *Int. J. Impact Eng.*, 23, 847
- Shuvalov, V. V., Artem'eva, N. A., Kosarev, I. B., Nemtchinov, I. V., & Trubetskaya, I. 1997, *Sol. Syst. Res.*, 31, 393
- Solem, J. C. 1994, *Nature*, 370, 349
- . 1995, *A&A*, 302, 596
- Svetsov, V. V. 1995, *Sol. Syst. Res.*, 29, 331
- Takata, T., & Ahrens, T. J. 1997, *Icarus*, 125, 317
- Takata, T., O'Keefe, J. D., Ahrens, T. J., & Orton, G. S. 1994, *Icarus*, 109, 3
- West, R. M., & Bönhardt, H., ed. 1995, *Proc. European Shoemaker-Levy 9 Conference* (ESO 52; Garching: ESO)
- Yabe, T., Aoki, T., Tajima, M., Xiao, F., Sasaki, S., Abe, Y., & Watanabe, J.-I. 1995, *Geophys. Res. Lett.*, 22, 2429
- Yabe, T., Xiao, F., Zhang, D. L., Sasaki, S., Kobayashi, N., & Terasawa, T. 1994, *J. Geomagn. Geoelectron.*, 46, 657
- Zahnle, K. J. 1992, *J. Geophys. Res.*, 97, 10243
- Zahnle, K., & Mac Low, M.-M. 1994, *Icarus*, 108, 1